ATP-induced asymmetric pre-protein folding: a potential driver of protein translocation?

Robin A. Corey[a], William J. Allen[a], Ian Collinson[a,1]

[a] School of Biochemistry, University of Bristol, University Walk, Bristol, BS8 1TD

[1] Corresponding author: ian.collinson@bristol.ac.uk

Keywords: SecA, SecYEG, protein translocation, molecular dynamics

Abstract

The transport of proteins across membranes is a fundamental and essential process, achieved in every cell by the 'Sec' translocon. In prokaryotes, SecY associates with the motor protein SecA to carry out ATP-driven pre-protein secretion – a vital step in the biogenesis of most periplasmic, outer membrane and secreted proteins. Structural data of the SecA-SecYEG complex has provided considerable insight into mechanism behind this process. Previously, we developed a Brownian ratchet model for protein translocation, whereby the free energy of ATP binding and hydrolysis favours the forward movement of pre-protein [Allen, Corey, Oately *et al. eLife* 2016]. Here, we use atomistic molecular dynamics simulation of a SecA-SecYEG complex engaged with pre-protein to address how this is achieved. The results provide an explanation of the underlying mechanism of protein transport. Our data reveals considerable pre-protein secondary structure, which demonstrates a nucleotide-dependent asymmetry across the channel. The data suggests that ATP-dependent pre-protein transport is partly driven by pre-protein secondary structure formation. The model previously described, and refined here, could easily be adapted for the transport of proteins across various other membranes, such as the endoplasmic reticulum and mitochondrial inner membrane.

Introduction

The compartmentalisation of cells necessitates that a considerable number of proteins need to be transported across membranes, mostly for secretion or organellar import. This process usually occurs before the nascent protein has folded. This paper explores how the folding process itself may be exploited to drive the protein translocation for the purposes of secretion.

The bulk of protein secretion is conducted by the ubiquitous Sec translocon, which also acts as the principle route for the insertion of membrane proteins. In bacteria, the translocon comprises SecY, SecE and usually SecG, with the protein-conducting pore through the centre of SecY. This complex can associate with either the ribosome for co-translational protein translocation (1) – the main pathway for nascent membrane protein insertion (2, 3) – or with the motor protein SecA for post-translational secretion (4). In the latter case the fully synthesised protein is maintained in an unfolded conformation by chaperones, such as SecB, and SecA itself (5, 6). The protein must then fold during or after the translocation process.

Post-translational translocation of the unfolded pre-protein occurs through a contiguous channel formed through SecA and SecY (Figure 1A-B; (7, 8)). The first step in this process is the ATP-dependent 'initiation' phase; whereby the pre-protein is targeted *via* its cleavable N-terminal signal sequence to SecA, and subsequently to the SecYEG complex. Transfer of the signal sequence to SecY unlocks the protein channel enabling the intercalation of the mature protein (9, 10). Next, the pre-protein is fed through the SecY channel in a process driven by both ATP and the proton motive force (PMF) (11). Finally, the signal sequence is cleaved and the pre-protein is either folded or trafficked onwards, *e.g.* to the outer membrane in gram-negative bacteria.

The SecY pore is pinched at its centre by a narrow constriction of six hydrophobic residues (8) (Figure 1A; blue mesh), which is flanked on the cytoplasmic and exterior sides by large solvated cavities, resulting in an hourglass-like shape (8) (Figure 1A). This ring is capped by the so-called 'plug' motif (8), which sits on the external face of the pore (Figure 1A; red helix) and helps to seal the channel against undesirable ion flux (12). Upon SecA binding, SecY rearranges to form a more open state (7), with this conformational switching likely controlled by the ATPase activity of SecA (13). This state still contains solvated cytoplasmic and exterior cavities, but the outwards movement of the plug and the insertion of the two-helix finger (2HF; Figure 1C) of SecA into the edge of the SecY cytoplasmic cavity profoundly changes the shape of the channel (Figure 1B). The 2HF has previously been shown to be coupled to the ATP binding region of SecA (the nucleotide binding site; NBS) (13-15), suggesting a possible nucleotide-dependent regulation of the SecY pore shape.

Recently, a pseudo-translocation state was captured by a crystal structure of *Geobacillus thermodentrificans* SecYE bound to *Bacillus subtilis* SecA (16). This was achieved by engineering a region of pre-protein into the SecA 2HF such that it resides within the SecY channel as a pre-protein would do. Amongst many observations, the structure reveals that the central pore of SecY tightly clasps the pre-protein (Figure 1 – figure supplement 1A).

We have previously provided evidence for a Brownian ratchet mechanism of ATP-driven protein secretion, where stochastic pre-protein diffusion is biased into directional force by the action of the SecA ATPase (13). We demonstrated that this ATPase activity was able to open and close the SecY channel, thus allowing/ preventing passage of specific regions of pre-protein, such as large or charged residues, or regions of secondary structure. Feedback from the SecA 2HF permitted control of this mechanism, providing the information input required for a biasing of Brownian motion (see Figure 8 and Video 1 from reference (13)).

Here, we present data extending this model to include structural changes within the translocating pre-protein. Atomic models were built based on the pre-protein-containing crystal structure (16), remodelled into a physiological system. Molecular dynamics (MD) simulation data reveal localised secondary structure formation in the pre-protein, within the SecY cavities. In the ATP-bound state, the degree of secondary structure is asymmetric between the cytoplasmic and exterior cavities. This asymmetry is not observed in the ADP-bound state, suggesting that pre-protein transport is, in part, driven by ATP-dependent secondary structure formation.

Results

Asymmetric secondary structure formation of the translocon-engaged pre-protein

The crystal structure 5EUL (16) was remodelled into a physiological complex (*i.e.* a non-fusion protein) containing SecA, SecYE and 76 residues of an unfolded pre-protein, hereafter referred to as SecA-SecYE-PP; the details of this remodelling are described in Figure 1 – figure supplement 1B-C and Table 1. This structure was built into a solvated POPC bilayer, and simulated over 1 µs with the NBS of SecA occupied with either ADP or ATP. The simulations were demonstrably stable within the core SecY region (Figure 2 – figure supplement 1) and, crucially, the SecY pore remained tightly formed around the bound pre-protein (Figure 2 – figure supplement 2A).

The most striking detail from the simulation data regards secondary structure within the pre-protein. In the region of the SecY channel, a range of hydrogen-bonded secondary structure motifs are observed, including considerable alpha-helix and 3_{10}-helix in the ATP and ADP simulations respectively (Figure 2 – figure supplement 2B). Visual inspection reveals considerable cross-pore asymmetry in this regard, with the majority of the secondary structure located in the exterior cavity (Figure 2A). This is present to some extent in both the ATP and ADP-bound complexes, but is approximately 2-fold higher for the ATP state (3.3 and 1.6 average residue count for ATP and ADP simulations over the final 500 ns of each simulation).

To better quantify this effect, further simulations were devised, aiming to maximise the information obtainable within current computational resource limits. Whilst much faster than tertiary structure folding, secondary structure formation is still reasonably slow in terms of atomistic simulation. Analysis of the initial trajectories (Figure 2 – figure supplement 2B) suggests that a time scale of ~100 ns is sufficient to kinetically

sample helix formation. This matches time scales previously reported for model protein folding (17), although it should be noted that any potential slower folding events, in the µs range, will not be sampled.

To provide broad conformational sampling and reduce any input bias from the starting configurations, multiple simulations were run from different starting coordinates. For this, new systems were modelled based on snapshots of the ADP- and ATP-bound systems at 1 µs. To abolish all of the secondary structure within the pre-protein, the 9 residues on each side of the central constriction were substituted with glycine and simulated for ~100 ns (Figure 2B), with the loss of structure confirmed using the dictionary of protein secondary structure (DSSP) algorithm (18, 19) (Figure 2 – figure supplement 3). Three snapshots that reported no secondary structure in this 18 residue region (Figure 2 – figure supplement 3– black circles) were chosen from each simulation for further analyses. For each of these snapshots, the 9 residues on each side of the central constriction were substituted with the same sequence (AFTHQRELE) in either a mirrored or tandem arrangement (Figure 2B). Then, 4-5 independent simulations were run for ~110 (+/- 30) ns each, for a total of ~3 µs of simulation data of both the ATP- and ADP-bound systems.

Due to sampling restrictions we were realistically only able to analyse a single 9 residue sequence. We opted to use the sequence from the original crystal structure, as this has already been shown to be stable in the SecY channel, thereby reducing potential for artefacts arising from changing the sequence. Additionally, the sequence has already been shown to fold within a reasonable time frame (Figure 2 – figure supplement 2B), and the ability to trap this sequence experimentally raises the possibility of direct comparison with experiment.

The 30 simulations for each nucleotide state were analysed for secondary structure in the 18 residue stretch of pre-protein through SecY. By quantifying the degree of hydrogen-bonded structure in the cytoplasmic and exterior cavities, a clear nucleotide-dependent effect is observed. In the ATP-bound simulations on average there is a >10 fold increase in pre-protein structure formation apparent in the exterior cavity compared to the cytoplasmic cavity (Figure 2C; blue data). This effect is not seen in the ADP-bound simulation data, wherein each cavity more closely resembles one another, and the cytoplasmic cavity in the ATP-bound state (Figure 2C; red data). Evidently, in the ATP bound state the influence exerted by the translocon on the folded state of the pre-protein is highly asymmetric; set up to promote folding on the exterior side of the channel. This asymmetry is not present in the ADP bound SecA-SecYEG complex (Figure 2 – figure supplement 4A-B).

Pre-protein folding is dependent on the translocon

Simulations were conducted in order to ensure that the starting configurations of the pre-protein were not biasing the behaviour of the pre-protein (described in Figure 2B). The coordinates for the unfolded 18 residue stretch were extracted from the simulation (using the mirrored sequence only) and built into separate water boxes, without either SecA-SecYE or the membrane. These were then treated in the same

way as the SecA-SecYE-PP simulations (simulated for 110 ns and each half analysed for secondary structure). The data show no significant asymmetry in pre-protein formation in either the simulation sets, be they derived from the ADP or ATP simulations (Figure 2 – figure supplement 4C). Therefore, the asymmetric secondary structure formation must be a consequence of the translocon, rather than the intrinsic properties of the pre-protein. Interestingly, comparison of the data with the translocon bound pre-protein, suggests that it is the cytoplasmic cavity that is precluding the folding process (Figure 2 – figure supplement 4C). In other words, the translocon applies an ATP-dependent break on the folding of the pre-protein at the cytosolic vestibule, rather than acceleration at the exterior.

Perturbed translational and rotational dynamics of waters within the SecY translocon

The thermodynamics and kinetics of protein folding can be affected by perturbed water dynamics (20), and the waters within SecY have previously been shown to exhibit reduced mobility (21). To examine the role of water in the pre-protein folding process, 31 structural snapshots were extracted from each of the 1 µs SecA-SecYE-PP ATP and ADP simulations for a broad conformational sampling. Short simulations were run using a statistical ensemble which accurately models rapid water dynamics (*i.e.* using an NVE ensemble – see Methods for details). For data analysis purposes only, a rectangular prism of 5x5x12 nm was imposed on each simulation box with its geometric centre on the SecY pore ring (Figure 3A). This prism was split into 24 slices of 0.5 nm along the z-axis, and the dynamics of the waters from each slice measured.

To measure the translational water dynamics, mean squared displacement (MSD) calculations were employed. MSD is a common statistical mechanics measure of translational motion. It follows the progression of an atom in relation to a reference position as a product of time, revealing the extent of its exploration of 3D space. When applied to the waters along an axis through SecA-SecYE-PP, there is a clear pattern of perturbation in the centre of SecY, with the water dynamics at the centre of the channel severely restricted (Figure 3B and Figure 3 – figure supplement 1). Comparison of the waters on either side of the pore reveal an asymmetry for the ATP-bound system – *i.e.* a higher degree of translational diffusion in the cytoplasmic cavity than the exterior cavity – but not in the ADP-bound system (Figure 3C).

The recorded perturbation of water dynamics resembles data previously reported for the resting translocon (21); and repeated here (Figure 3 – figure supplement 2). As the resting translocon has a cross-channel symmetry akin to that of the ADP-bound state, these new results suggest that the asymmetry is somehow imposed upon ATP binding at SecA.

In addition to the translational dynamics, rotational water dynamics were determined by computation of the corresponding dipole moments during the simulations. These data can be modelled using an autocorrelation function C(t), which equals the degree of correlation of the dipoles at each time *t* in relation to the zero time point. As previously recorded (21), the waters at the centre of the translocon are too

perturbed to accurately measure the rotational dynamics (Figure 3 – figure supplement 3)

Folding of pre-protein and localised water dynamics in bulk solvent

To probe the apparent correlation between an increased propensity for pre-protein secondary structure formation (Figure 2C) and reduced translation water dynamics (and *vice versa*) (Figure 3B), we modelled peptide folding in constrained bulk solvent. For this, we applied positional restraints to the waters in a peptide-water simulation box, with the strength of the positional restraint chosen to simulate the reported MSD values for the water in the SecY cavities (cytoplasmic cavity = 21 kJ mol^{-1} nm^{-2}; exterior cavity = 92 kJ mol^{-1} nm^{-2}; Figure 3 – figure supplement 4A-B). Intriguingly, we see the opposite effect to that expected from Figure 2: the more ordered water results in a 4-5 fold decrease in secondary structure formation (Figure 3 – figure supplement 4C). This is a plausibly an effect of the higher-ordered water restricting the fluctuation (RMSF) of the peptide (Figure 3 – figure supplement 4D), *i.e.* the kinetics of pre-protein folding are slowed by ordered water, but not necessarily the thermodynamics. However, extension of 6 simulations for each condition to ~400-450 ns fails to change the observed effect (Figure 3 – figure supplement 4E).

These data suggest that ordering of water does not drive the folding process. It seems plausible that it is instead the folding of the pre-protein itself is causing the water ordering. To test this, a single folding trajectory (from Figure 3 – figure supplement 4C) that samples a range of unfolded and folded peptide configurations was taken. A number of snapshots along this trajectory were selected and equilibrated, with restraints on the protein but not on the water molecules. NVE simulations were run using the same restraints, and the computed water dynamics were compared to the recorded level of structure (Figure 3 – figure supplement 4F). Fitting a linear regression to the data reveals a statistically significant increase in water ordering with protein secondary structure, confirming that pre-protein folding is perturbing the water dynamics rather than the other way around. Thus, the perturbed water structure is a consequence of pre-protein folding, rather than a driving force for folding.

Nucleotide dependent variation in the geometry of the exterior and interior cavities translocon

The conformational entropy of a protein's extended state is reduced when in a confined space, which should favour more compact, folded states (22). This raises the possibility that ATP-driven opening of the SecY translocon (13) might have a direct impact on pre-protein secondary structure. To test this, the cavity sizes of the translocons associated with either ADP or ADP were assessed throughout the 1 µs simulations. The pre-protein was removed from the translocon and the dimensions of the cavities on either side were measures from 31 structural snapshots from each simulation using the HOLE program (23). For consistency, the analyses were initiated at a set point between the residues Ile-78 and Ile-275 at the centre of the

SecY pore (see Figure 1 – figure supplement 1A). In all of the simulation snapshots, a channel through SecY is found, and in many a channel through the whole complex can be traced (Figure 4 – figure supplement 1).

The cavity volumes were measured from the constriction at the centre of the SecY pore and 6.5 Å either towards the cytosol (inside) or exterior (Figure 4A and Figure 4 – figure supplement 2A). The relative sizes of these defined regions reveal a strong asymmetry between cytoplasmic and exterior cavities in the ATP-bound simulations (Figure 4B; blue data); in contrast, the ADP associated complexes simulations were symmetrical in this respect (Figure 4B; red data). The larger cytosolic cavity of the ATP associated translocon might be responsible for the reduced propensity for pre-protein folding.

Whilst it is difficult to deduce the precise mechanism for ATP-induced increase in the cavity size of the exterior cavity, one candidate arising from the simulation data is the 2HF, at the SecA-SecY interface (Figure 1C). The 2HF inserts into the SecY channel (7), contacts the translocating pre-protein (24, 25) and has a key, albeit disputed, role in protein translocation (13-15, 26, 27). In the simulation data, the distance from the tip of the 2HF to the central pore of SecY is substantially larger in the ATP state than in the ADP state (Figure 4 – figure supplement 2B-C), providing a plausible mechanism for how the machinery regulates the size of its cytoplasmic cavity.

Cavity size regulation occurs in the absence of pre-protein

To test whether the ATP-driven increase in size of the cytosolic chamber (Figure 4) is dependent on pre-protein, we analysed previously-produced simulation data (13) of the SecYEG-SecA complex (PDB code 3DIN(7)) with ATP and ADP bound, but without pre-protein (13). These systems proved challenging, as the HOLE program was unable to locate the correct cavity in 8/31 of the simulations of the translocon associated with ATP, and 20/31 of those associated with ADP. Comparison of the snapshots in which HOLE succeeded, however, revealed the same effect is seen as before: the cytoplasmic cavity of SecY is much larger than the periplasmic cavity in the ATP-bound state, while there is no difference in the ADP-bound state (Figure 4 – figure supplement 3). Evidently, the cytoplasmic cavity opens up in response to ATP irrespective of the presence of pre-protein.

Secondary structure formation prevents transit through SecY pore

To determine whether the pre-protein secondary structures observed here impede passage through the SecY pore, a series of steered MD simulations were executed. Here, a directional pulling force was applied to a stretch of the pre-protein through SecYE, with SecA and the rest of the pre-protein removed (Figure 5A). The pre-protein either contained a helical region – as sampled by equilibrium MD in the ATP-bound state (Figure 2, S3B), and stabilised here using a distance restraint between positions *i* and *i+4* – or, had the helix abolished using a short steered MD simulation. These two substrates were pulled through the SecY pore, and the passage time of

10 independent repeats recorded. It was observed that the helix-containing substrate took considerably longer to pass (~10 fold slower) than the other (Figure 5B). Whilst this setup clearly does not represent the physiological translocation process, the data indicate a significant barrier to the transit of folded regions of pre-protein through the translocon channel.

Discussion

While it is widely accepted that pre-proteins need to be unfolded during transport (5, 6), this is only with respect to tertiary structure. A high degree of secondary structure has been reported for extended pre-proteins as they exit the ribosome (28, 29), and many proteins fold further once through to the periplasm (30). Furthermore, previous studies have intimated that pre-protein can form secondary structure within the translocon (25, 31). Here, we have performed a set of computational analyses on a model of a SecA-SecYE complex engaged with pre-protein (SecA-SecYE-PP), aimed at elucidating the importance of pre-protein secondary structure to transport.

Our data reveal a strong propensity for the pre-protein to form secondary structure both on the cytosolic and periplasmic sides of the channel. Strikingly, when ATP – but not ADP – is bound to SecA, this propensity is asymmetric: α-helix becomes more prevalent in the exterior cavity than in the cytoplasmic cavity (Figure 2). The asymmetry is not appreciably driven by water dynamics; rather, our data suggest that is comes primarily from changes in the geometry of the cavities in SecY.

It has previously been suggested that confinement of a protein can promote protein folding, by reducing the entropy of the unfolded state (22). This works because secondary structure formation is essentially dictated by a balance between entropy and enthalpy: the unfolded state has higher entropy than the folded state, but this is offset by the enthalpic gain from backbone hydrogen bonding (32). Our data provide empirical support for this assertion: significantly more pre-protein secondary structure is observed in the more confined periplasmic cavity.

In our analyses, however, cavity size is not sufficient to explain the large differences in secondary structure formation. In the ADP-bound state, both cavities have a similar volume to the tight periplasmic cavity in the ATP-bound state – but this is not accompanied by an increase in pre-protein folding. This might simply be due to subtle effects not picked up in our analyses. Alternatively, it might be due to the complex nature of the confinement effect on folding kinetics and thermodynamic stability (33, 34). Either way, the ADP-bound state fails to report the level of secondary structure formation of the ATP-bound state.

Our data clearly reveal an ATP-dependent increased propensity for pre-protein folding at the exit site of the SecYEG channel. This is achieved by an ATP-dependent increase in volume of the cytosolic cavity (Figure 4B) and reduction in the amount of secondary structure within it (Figure 2C). Steered MD simulations confirm that regions of secondary structure are much less likely to pass the narrow SecY pore (Figure 5). Taken together, these effects could contribute significantly to any translocation model that incorporates pre-protein diffusion through the channel (13,

14). In our previously proposed Brownian ratchet model (13), ATP binding is triggered by the presence of bulky regions – most likely secondary structure – at the cytosolic entrance to SecY. If this ATP binding simultaneously unwinds pre-protein secondary structure in the cytoplasmic cavity of the channel, while not affecting folding in the exterior cavity, it would contribute significantly to the direction of diffusion (for a model of how this might work, see Figure 6).

It should be noted that we have largely ignored pre-protein sequence for this study, due to sampling restrictions within MD. The model protein from which our sequence was derived, pro-OmpA, eventually folds into a β-barrelled conformation, so the formation of α-helices could be considered surprising. However, the impact of non-local factors on the secondary structure of proteins is well-established (35), so an α-helix could easily be formed temporarily then broken in the absence of the final β-contacts. In addition, the fact that this sequence is able to sit stably in crystal structure suggests that it represents a local minimum on the energy landscape. Most probably, different protein sequences will have different helical propensities – only some will require ATP to facilitate their passage through the channel.

Experimental validations of the findings reported here are difficult to achieve, as the ADP-bound complex is difficult to stabilise for structural analysis and the complexity of the translocation process makes it hard to disentangle the relevant effects from altering the pre-protein sequence. Nevertheless, we feel that the data presented here are compelling, and reveal considerable insight into the translocation process. Any model for Sec-mediated pre-protein translocation should take into consideration a possible input from pre-protein secondary structure.

Methods

Molecular dynamics simulations

All simulations were run using GROMACS 5.0.4 or 5.1.2 (36). Models for the simulations were built using chains A, Y and E of the crystal structure 5EUL (16) as starting coordinates, with missing loops added using Modeller (37), either modelling unstructured loops or modelled based on previous coordinates of SecA-SecYEG (PDB code 3DIN; (7)). Due to the non-physiological arrangement of the SecA 2HF and the pre-protein substrate of the input model, the 2HF was modelled based on 3DIN, and the substrate was extended in an unfolded conformation through the SecA, *via* known crosslinking sites (24). Substrate building was done with PyMOL (38). In the SecA NBS, the ADP-BeFx molecules were replaced with either ADP or ATP (39). Alternatively, simulations were built using the *M. jannaschii* SecYEβ crystal structure (8).

The protein and solvent atoms were described in the OPLS all-atom force field (40), with the simulations being run in an OPLS united-atom POPC membrane (41). The protein-membrane structures were built into simulation boxes with periodic boundary conditions in all dimensions and solvated with explicit SPC water and sodium and chloride ions to a neutral charge and concentration of 0.15 M. For the 1 µs SecA-SecYE-PP and *M. jannaschii* SecYEβ simulations, the systems were energy minimized using the steepest descents method over 2 x 5,000 steps, then

equilibrated with positional restraints on heavy atoms for 1 ns in the NPT ensemble at 300 K with the Bussi-Donadio-Parrinello thermostat (42) and semi-isotropic Parrinello-Rahman pressure coupling (43, 44). Production simulations were run without positional restraints with 2 fs time steps over 500-1 µs on the UK HPC facility ARCHER, using time awarded by HECBioSim. Bond lengths were constrained using the LINCS method. Non-bonded interaction cut-offs were calculated using the Verlet method, with the neighbour search list updated every 20 steps. Long-range electrostatic interactions were calculated using the particle mesh Ewald method and a cut-off of 1.0 nm was applied for van der Waals and short range electrostatic interactions. All simulations reached a steady state as judged by their root-mean-squared-deviation from the starting structure (Figure 4 – figure supplement 1).

Secondary structure formation analyses

Formation of secondary structure was determined both using visual analysis and quantified using the dictionary of secondary structure of proteins (DSSP) algorithm (18, 19). This was implemented using the Gromacs utility do_dssp, which provides an estimation of secondary structure for each reside based on dihedral angle, including 'no structure', 'α-helix', '3_{10}-helix' and 'hydrogen-bonded turn'.

Extending simulations to investigate secondary structure formation

To reduce the likelihood of sequence-dependent bias in the simulation data, a stretch of 9 residues on either side of the SecY pore was modelled as a mirror image repeat or in tandem. The sequence used (AFTHQRELE) was chosen is this was the sequence from the initial crystal coordinates. This means that the sequence is already known to sit happily within the translocon, and makes comparison to experimental data more straightforward. Initially, this 18 residue stretch was modelled as poly-glycine using SCWRL4 (45) in order to destroy the exiting secondary structure. Following steepest descents energy minimization and 1 ns equilibration, production runs were carried out until all of the secondary structure within this region had been abolished, as according to DSSP analysis (19); ~110 ns for the ATP-bound complex and ~80 ns for the ADP-bound complex (Figure 2 – figure supplement 3). For each simulation, three time points (70, 80 and 110 ns for ATP and 50, 65 and 80 ns for ADP) were chosen which displayed no structure at all according to DSSP analysis (Figure 2 – figure supplement 3A). This represents a reasonably broad configurational sampling, and prevents the analyses being too biased by a specific starting configuration.

For each time point, the 18 residue region was modelled to either ELERQHTFAAFTHQRELE or ELERQHTFAELERQHTFA using SCWRL4 (45), minimised using steepest descents, equilibrated for 1 ns and simulated for between 90 and 110 ns. The final 75 ns of each simulation run were then analysed for secondary structure. Simulations were run, in part, on EPCC's Cirrus HPC Service.

Water dynamics simulations

To model the water dynamics in and around the translocon, a series of simulations were run using structural snapshots of the 1 µs SecA-SecYE-PP ATP simulation from Figure 2 as starting points (500, 502, 504, 506, 508, 510, 600, 602, 604, 606,

608, 610, 700, 702, 704, 706, 708, 710, 800, 802, 804, 806, 808, 810, 900, 902, 904, 906, 908, 910, 1000 ns). Water dynamics simulations were run in the NVE ensemble, meaning a constant number of particles, volume and energy were maintained throughout. The advantage of this is to avoid introduction of artificial perturbations through use of a thermostat or barostat. Simulations were run with a 1 fs time step, writing coordinates every 5 fs. The Verlet cutoff scheme was used with a buffer size of 0.001 kJ mol^{-1} ps^{-1} to achieve proper energy conservation, as monitored through following the energy of the simulations. Simulations were run on the University of Bristol's High Performance Computer, BlueCrystal.

Mean squared displacement calculations

To model the translational dynamics of the waters in the system, mean squared displacement (MSD) calculations were employed. Analyses were carried out as described previously (21). Briefly, a box of 5x5x12 nm was built around SecY, with the geometric centre at the pore ring. This box was subdivided into 24 slices of 0.5 nm, and the waters from each slice were analysed separately. The MSD of the waters in each slice was plotted, and the last 25 ps was fitted to a power law equations (Equation 1).

Equation 1.

$$MSD(t) = k * t^{A}$$

Where *k* is a fitting parameter, and the exponent *A* provides information on the molecular diffusivity. From this, the *A* value was plotted for each slice.

SDAC calculations

To calculate the rotational dynamics of the waters, the same slices as used for the MSD calculations were subjected to SDAC calculations. Here, the data is modelled using an autocorrelation function C(t), which equals the degree of correlation of the dipoles at each time *t* in relation to the zero time point. For each data set, C(t) can be fitted to an exponential decay function, and the time at which the function reaches 1/*e* can be calculated, and plotted for each slice.

Folding in bulk solvent with positional restraints

Waters dynamics in solvent boxes with 0.15 M NaCl were probed at a range of different water orders, as determined using MSD analyses. For this, restraining forces in the range of 0 to 1000 kJ mol^{-1} nm^{-2} were applied to the oxygen of each water molecule, and 100 ns simulations were run in the NPT ensemble, with isotropic pressure coupling. Snapshots were taken at 50, 60, 70, 80, 90 and 100 ns, and additional 50 ps simulations were run in the NVE ensemble. These simulations were analysed for translational water dynamics as described above, with the output plotted as a titration curve of restraining force *vs.* translational diffusion. The MSD values for the waters in the periplasmic and cytoplasmic cavities were read off of this curve.

Using the force constants representing water ordering in the periplasmic and cytoplasmic cavities, protein folding simulations were run of a peptide

(ELERQHTFAAFTHQRELE) in an extended configuration. The setup of these followed the same technique as for the simulations in the main part of the study, except that equilibration was achieved through 10 ps NVT simulation with 0.5 fs time steps, 100 ps NVT simulation with 2 fs time steps and 100 ps NPT simulation with 2 fs time steps. Then, 100 ns production simulations were run, with secondary structure formation within the pre-protein analysed using DSSP.

Folding in bulk solvent

Additional folding simulations were run and analysed as described above but without positional restraints on the water molecules, and instead of extended configuration for the peptide, coordinates were extracted from the simulations with the poly-glycine region in the translocon (Figure 3 – figure supplement 2).

HOLE

To analyse the SecY cavity sizes, snapshots were taken from the 1 µs SecA-SecYE-PP ATP and ADP simulations at 500, 502, 504, 506, 508, 510, 600, 602, 604, 606, 608, 610, 700, 702, 704, 706, 708, 710, 800, 802, 804, 806, 808, 810, 900, 902, 904, 906, 908, 910 and 1000 ns. In addition, snapshots were taken at the same time points from simulations previously published (13) of the SecA-SecYEG complex without pre-protein, with ATP or ADP bound.

For each snapshot, the centre of the SecY channel was initially defined as the geometric centre of the pore ring residues, and this was used to seed the HOLE calculations. The correct siting of the cavity was determined with visual inspection using VMD(46). For the successful calculations, data were extracted for 6.5 Å on either side of the pore ring. The area under the curves were computed and integrated using the trapezoidal rule with partitions of 0.5 Å.

Steered MD

A 1 µs snapshot was taken from the SecA-SecYE-PP ATP-bound simulation, in which four pre-protein residues in the exterior SecY cavity form an alpha-helical configuration (Figure 2A). From this, SecA was removed and the backbone of the pre-protein was broken at residue Y1253 and removed from residue G1270 onwards (Figure 5A), and simulated for 5 ns. The alpha-helix was then either forced into an unstructured conformation using steered MD with a pulling force of 1000 kJ mol^{-1} nm^{-1} for 36 ps on residue E1260 or stabilised using a constraint of 0.2-0.25 nm between the backbone CO of residue 1262 and NH of 1266, followed by 5 ns unbiased simulation. Then, 10 independent steered MD simulations were run for each state, where the substrate was pulled from residue G1270 in a z-axis direction using a force constant of 600 kJ mol^{-1} nm^{-1}. DSSP analysis confirmed that the helix remained formed or broken accordingly throughout the simulation. For each repeat, the time take for the helical/non-helical region to cross the pore was measured, based on the centre-of-mass distance between the region and the SecY pore residues, Ile-78, Ile-183, Ile-275 and Ile-404 (*G. thermodentrificans* numbering).

Acknowledgements

This work was funded by the BBSRC: BB/M003604/1, BB/I008675/1 and BB/N015126/1 and Wellcome Trust: 104632. This work was carried out using the computational facilities of the Advanced Computing Research Centre, University of Bristol (http://www.bris.ac.uk/acrc/). Additional simulations were carried out using computer time on EPCC's Cirrus HPC Service (https://www.epcc.ed.ac.uk/cirrus) and on the ARCHER UK National Supercomputing Service (http://www.archer.ac.uk), provided by HECBioSim, the UK High End Computing Consortium for Biomolecular Simulation (hecbiosim.ac.uk), supported by the EPSRC.

References

1. Blobel G & Dobberstein B (1975) Transfer of proteins across membranes. I. Presence of proteolytically processed and unprocessed nascent immunoglobulin light chains on membrane-bound ribosomes of murine myeloma. *The Journal of Cell Biology* 67(3):835-851.
2. Muller M, Koch HG, Beck K, & Schaefer U (2001) Protein traffic in bacteria: Multiple routes from the ribosome to and across the membrane. *Prog Nucleic Acid Re* 66:107-157.
3. Jungnickel B, Rapoport TA, & Hartmann E (1994) Protein translocation: common themes from bacteria to man. *FEBS letters* 346(1):73-77.
4. Hartl FU, Lecker S, Schiebel E, Hendrick JP, & Wickner W (1990) The Binding Cascade of Secb to Seca to Secy/E Mediates Preprotein Targeting to the Escherichia-Coli Plasma-Membrane. *Cell* 63(2):269-279.
5. Arkowitz RA, Joly JC, & Wickner W (1993) Translocation can drive the unfolding of a preprotein domain. *EMBO J* 12(1):243-253.
6. Bonardi F*, et al.* (2011) Probing the SecYEG translocation pore size with preproteins conjugated with sizable rigid spherical molecules. *Proc Natl Acad Sci U S A* 108(19):7775-7780.
7. Zimmer J, Nam Y, & Rapoport TA (2008) Structure of a complex of the ATPase SecA and the protein-translocation channel. *Nature* 455(7215):936-943.
8. Van den Berg B*, et al.* (2004) X-ray structure of a protein-conducting channel. *Nature* 427(6969):36-44.
9. Corey RA*, et al.* (2016) Unlocking the bacterial SecY translocon. *Structure* 24(4):518-527.
10. Hizlan D*, et al.* (2012) Structure of the SecY complex unlocked by a preprotein mimic. *Cell reports* 1(1):21-28.
11. Brundage L, Hendrick JP, Schiebel E, Driessen AJM, & Wickner W (1990) The purified E. coli integral membrane protein SecYE is sufficient for reconstitution of SecA-dependent precursor protein translocation. *Cell* 62(4):649-657.
12. Park E & Rapoport TA (2011) Preserving the membrane barrier for small molecules during bacterial protein translocation. *Nature* 473(7346):239-242.
13. Allen WJ*, et al.* (2016) Two-way communication between SecY and SecA suggests a Brownian ratchet mechanism for protein translocation. *eLife* 5:e15598.
14. Bauer BW, Shemesh T, Chen Y, & Rapoport TA (2014) A "Push and Slide" Mechanism Allows Sequence-Insensitive Translocation of Secretory Proteins by the SecA ATPase. *Cell* 157(6):1416-1429.
15. Whitehouse S*, et al.* (2012) Mobility of the SecA 2-helix-finger is not essential for polypeptide translocation via the SecYEG complex. *J Cell Biol* 199(6):919-929.

16. Li L*, et al.* (2016) Crystal structure of a substrate-engaged SecY protein-translocation channel. *Nature*.
17. Davis CM, Cooper AK, & Dyer RB (2015) Fast helix formation in the B domain of protein A revealed by site-specific infrared probes. *Biochemistry* 54(9):1758-1766.
18. Kabsch W & Sander C (1983) Dictionary of protein secondary structure: pattern recognition of hydrogen-bonded and geometrical features. *Biopolymers* 22(12):2577-2637.
19. Joosten RP*, et al.* (2011) A series of PDB related databases for everyday needs. *Nucleic Acids Res* 39(Database issue):D411-419.
20. Lucent D, Vishal V, & Pande VS (2007) Protein folding under confinement: a role for solvent. *Proceedings of the National Academy of Sciences* 104(25):10430-10434.
21. Capponi S, Heyden M, Bondar AN, Tobias DJ, & White SH (2015) Anomalous behavior of water inside the SecY translocon. *Proc Natl Acad Sci U S A* 112(29):9016-9021.
22. Zhou H-X & Dill KA (2001) Stabilization of proteins in confined spaces. *Biochemistry* 40(38):11289-11293.
23. Smart OS, Neduvelil JG, Wang X, Wallace B, & Sansom MS (1996) HOLE: a program for the analysis of the pore dimensions of ion channel structural models. *Journal of molecular graphics* 14(6):354-360.
24. Bauer BW & Rapoport TA (2009) Mapping polypeptide interactions of the SecA ATPase during translocation. *Proceedings of the National Academy of Sciences of the United States of America* 106(49):20800-20805.
25. Zhang Q*, et al.* (2017) Alignment of the protein substrate hairpin along the SecA two-helix finger primes protein transport in Escherichia coli. *Proceedings of the National Academy of Sciences*:201702201.
26. Erlandson KJ*, et al.* (2008) A role for the two-helix finger of the SecA ATPase in protein translocation. *Nature* 455(7215):984-987.
27. Collinson I, Corey RA, & Allen WJ (2015) Channel crossing: how are proteins shipped across the bacterial plasma membrane? *Philos Trans R Soc Lond B Biol Sci* 370(1679).
28. Lu J & Deutsch C (2005) Folding zones inside the ribosomal exit tunnel. *Nat Struct Mol Biol* 12(12):1123-1129.
29. Hardesty B & Kramer G (2001) Folding of a nascent peptide on the ribosome. *Prog Nucleic Acid Res Mol Biol* 66:41-66.
30. Antonoaea R, Fürst M, Nishiyama K, & Müller M (2008) The periplasmic chaperone PpiD interacts with secretory proteins exiting from the SecYEG translocon. *Biochemistry* 47(20):5649-5656.
31. Gumbart J, Chipot C, & Schulten K (2011) Free energy of nascent-chain folding in the translocon. *Journal of the American Chemical Society* 133(19):7602-7607.
32. Richardson JM, Lopez MM, & Makhatadze GI (2005) Enthalpy of helix–coil transition: Missing link in rationalizing the thermodynamics of helix-forming propensities of the amino acid residues. *Proceedings of the National Academy of Sciences of the United States of America* 102(5):1413-1418.
33. Takagi F, Koga N, & Takada S (2003) How protein thermodynamics and folding mechanisms are altered by the chaperonin cage: molecular simulations. *Proceedings of the National Academy of Sciences* 100(20):11367-11372.
34. Rathore N, Knotts TA, & de Pablo JJ (2006) Confinement effects on the thermodynamics of protein folding: Monte Carlo simulations. *Biophysical journal* 90(5):1767-1773.
35. Minor Jr DL & Kim PS (1996) Context-dependent secondary structure formation of a designed protein sequence. *Nature* 380(6576):730.
36. Berendsen HJC, van der Spoel D, & van Drunen R (1995) GROMACS: A message-passing parallel molecular dynamics implementation. *Computer Physics Communications* 91(1–3):43-56.

37. Sali A & Blundell TL (1993) Comparative protein modelling by satisfaction of spatial restraints. *Journal of molecular biology* 234(3):779-815.
38. Delano WL (2002) The PyMOL Molecular Graphics System.
39. Piggot TJ, Sessions RB, & Burston SG (2012) Toward a Detailed Description of the Pathways of Allosteric Communication in the GroEL Chaperonin through Atomistic Simulation. *Biochemistry* 51(8):1707-1718.
40. Jorgensen WL, Maxwell DS, & Tirado-Rives J (1996) Development and Testing of the OPLS All-Atom Force Field on Conformational Energetics and Properties of Organic Liquids. *Journal of the American Chemical Society* 118(45):11225-11236.
41. Ulmschneider JP & Ulmschneider MB (2009) United Atom Lipid Parameters for Combination with the Optimized Potentials for Liquid Simulations All-Atom Force Field. *Journal of chemical theory and computation* 5(7):1803-1813.
42. Bussi G, Donadio D, & Parrinello M (2007) Canonical sampling through velocity rescaling. *J Chem Phys* 126(1):014101.
43. Parrinello M & Rahman A (1981) Polymorphic transitions in single crystals: A new molecular dynamics method. *Journal of Applied Physics* 52(12):7182-7190.
44. Nosé S & Klein ML (1983) Constant pressure molecular dynamics for molecular systems. *Molecular Physics* 50(5):1055-1076.
45. Krivov GG, Shapovalov MV, & Dunbrack RL, Jr. (2009) Improved prediction of protein side-chain conformations with SCWRL4. *Proteins* 77(4):778-795.
46. Humphrey W, Dalke A, & Schulten K (1996) VMD: visual molecular dynamics. *Journal of molecular graphics* 14(1):33-38.

Figures

Figure 1: Structures of SecYEG and SecA.

Views of A) SecYEβ (PDB 1RHZ; (8)) and B) SecYEG-SecA (PDB 3DIN; (7)) showing the cavities through the channel, with the protein in grey surface, the pre-protein pore constrictions in blue (SecY) or purple (SecA) mesh, and the SecY plug in red helix. The image was produced by embedding the crystal structures in a POPC membrane, solvating with explicit waters and allowing the non-heavy atoms to relax through restrained molecular dynamics (MD) over 4 ps. Degree of solvation and water density in the channel to be considered for illustrative purposes only.

C) Cartoon of SecA-SecYEG with an engaged pre-protein, modelled from PDB 5EUL (16). The Sec subunits are shown as cartoon with mesh overlay, with SecY in light pink, SecE orange, and SecA light-blue, with the 2HF highlighted. The unfolded pre-protein is shown in dark blue, labelled ‘PP’. The ATP analogue is coloured as orange, blue and red spheres. The approximate position of the membrane is marked.

Figure 2: ATP-dependent asymmetric folding of pre-protein in the Sec translocon

A) Cartoon representation of a 1 µs MD snapshot of the SecA-SecYE-PP complex in the ATP-bound state, coloured as per Figure 1C. A region of alpha-helix, as computed by the dictionary of secondary structure of proteins (DSSP) and confirmed visually, is highlighted in red mesh. The approximate position of the membrane is shown in grey.

B) Showing the work-flow to produce the pre-protein folding data. An 18-residue stretch of pre-protein is substituted to 18-Gly, then to a 9 residue stretch from the input model, repeated either mirrored or in tandem. The simulation times for each step are shown above.

C) The degree of pre-protein folding in the exterior and cytoplasmic cavities of SecY in the ADP and ATP states. Shown are the datasets for both the mirrored and tandem repeats of the substrate. Error bars are s.e.m, and reported significance is from two-tailed *t*-tests, where $p < 0.0001$ for both ATP sets, and $p = 0.394$ and 0.080 for the mirrored and tandem ADP simulations respectively.

Figure 3: Perturbed water dynamics throughout the Sec translocon

A) Cartoon showing the prism of waters analysed for translational and rotational dynamics. The waters are shown as blue surface, alternating light and dark blue for the pooled data analysis in panel C. Note that whilst the membrane and solvent outside of this prism are missing from this figure, they were present in the simulation.

B) MSD data of the waters along the length of the protein. The average MSD was calculated for each 0.5 nm slice, the data fitted to a power law equation, and the power value (A) for each slide was averaged across all 31 simulations. Here, the average for each slice is shown, with s.e.m as error bars. Both the ATP and ADP simulations are perturbed in the centre of SecY, but the ATP appears to be perturbed in an asymmetric manner.

C) The values from panel B are pooled by region of the system, as illustrated by light and dark blue colouring in panel A, and the data plotted as box and whisker plots showing upper quartile, median and lower quartile.

Figure 4: Perturbed water dynamics throughout the Sec translocon

A) Representative HOLE data used for averaging analysis. The protein backbone is shown as coloured trace and the calculated cavity as blue mesh. The central coordinate from the HOLE program is shown as a green line. On the left is the data at 608 ns of the ATP simulations, and on the right is at 610 ns of the ADP simulation.

B) Quantified cavity sizes from the ATP and ADP simulation data. Plotted are the median and interquartile range. The difference between the exterior and cytoplasmic cavities was tested against an unpaired two-tailed *t*-test, reporting *p* values of <0.0001 and 0.1264 for ATP and ADP respectively.

Figure 5: Pre-protein secondary structure prevents transit through SecY

A) Cartoon illustrating the principle behind the steered MD simulations. From a 1 µs snapshot of ATP-bound SecA-SecYE-PP, SecYE and a short region of helix-containing pre-protein were extracted, with the membrane trimmed to size. Two

configurations of the pre-protein were established: either the helix was stabilised by a distance restraint between the hydrogen bonded atoms, or the helix was broken by a short steered MD simulation pulling the ends apart. A backward pulling force was then applied to each pre-protein, and the time taken to pass the channel measured

B) Data from the simulations described in A. The presence of a helix in the pre-protein appears to be enough to restrict passage though the pore, $p = 0.0045$ using a two-tailed *t*-test.

Figure 6: A model for pre-protein translocation through SecA-SecYEG

In this model, SecA is shown in light blue, SecYEG in red, the SecY central cavity in orange and the pre-protein in dark blue. The direction of pre-protein diffusion is shown with a coloured arrow (green = forwards, red = backwards and orange = either).

The starting state (in the dashed box) represents the ADP-bound complex with no pre-protein secondary structure. In this state, the pre-protein is free to diffuse freely backwards and forwards, so no net translocation occurs. Then, localised pre-protein secondary structure formation can occur in either the exterior or cytoplasmic cavity; structure in the exterior cavity favours forward – productive – diffusion (top left panel), whereas structure in the cytoplasmic cavity would favour backward diffusion (bottom left panel). We previously demonstrated that bulky pre-protein in the cytoplasmic cavity triggers nucleotide exchange (13), resulting in the bottom right state, where ATP is bound and the cytoplasmic cavity has widened. As shown in Figure 2, this state strongly disfavours secondary structure in the cytoplasmic cavity, driving the complex towards the middle right panel. Here, either ATP is immediately hydrolysed, to return to the original state, or secondary structure forms in the exterior cavity (as per the top right panel), resulting in a forward diffusion of pre-protein.

In this way, ATP is acting to prevent the backward diffusion of pre-protein in the complex, by shifting the equilibrium towards the top states (yellow arrow).

Figure 1

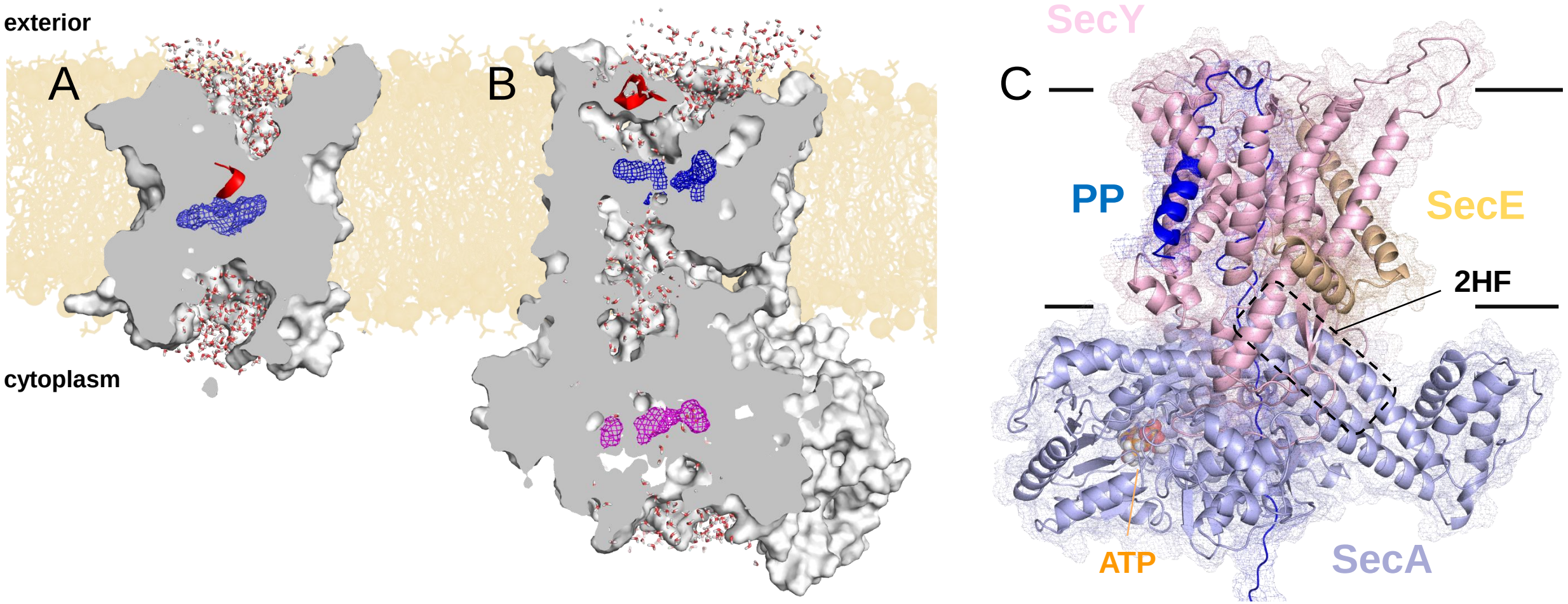

Figure 2

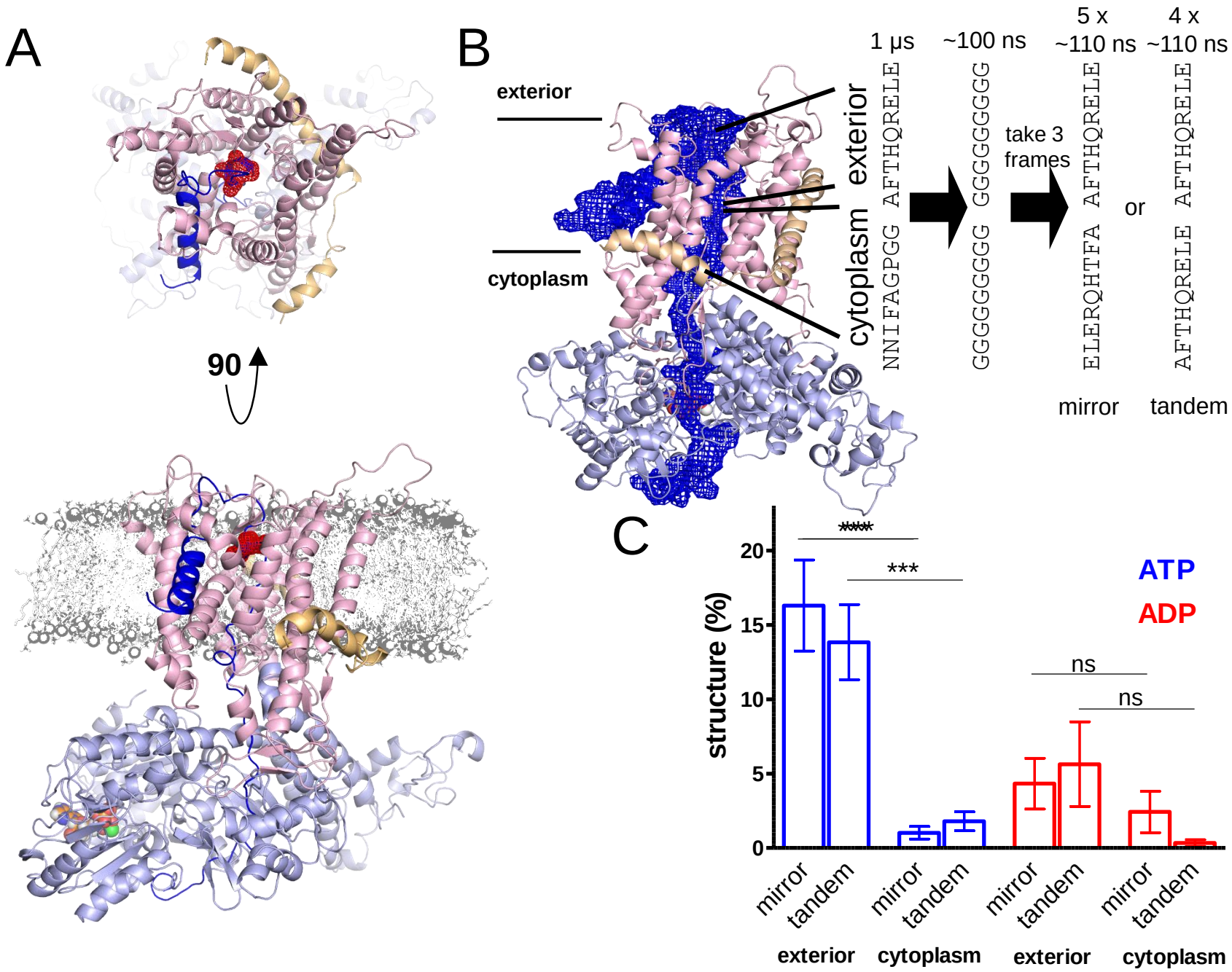
A
90
B
exterior
cytoplasm
1 µs
~100 ns
5 x
~110 ns
4 x
~110 ns
exterior
cytoplasm
NNIFAGPGG AFTHQRELE
GGGGGGGGG GGGGGGGGG
ELERQHTFA AFTHQRELE
AFTHQRELE AFTHQRELE
take 3
frames
or
mirror
tandem
C
structure (%)
20
15
10
5
0
****
***
ns
ns
ATP
ADP
mirror
tandem
mirror
tandem
mirror
tandem
mirror
tandem
exterior
cytoplasm
exterior
cytoplasm

Figure 3

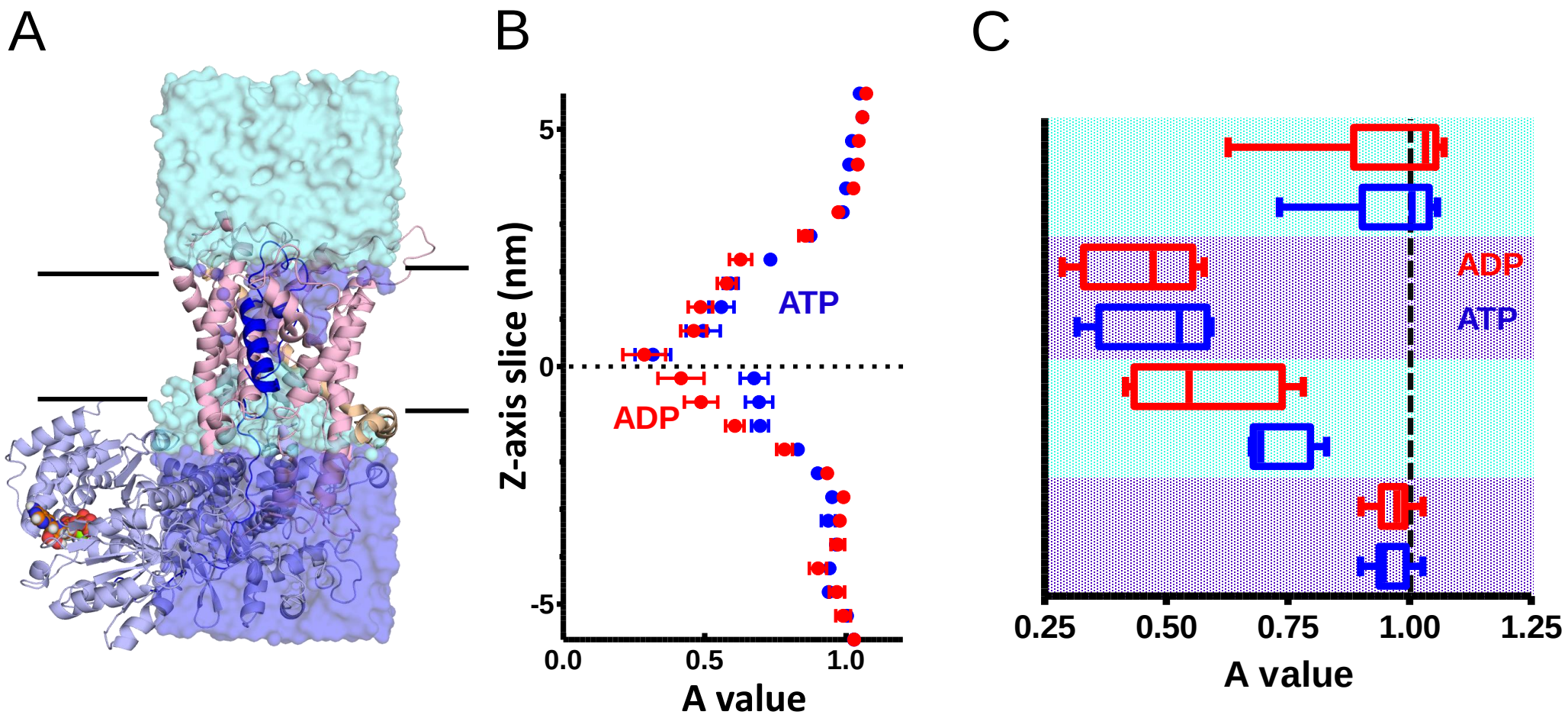
A
B
C
5
0
-5
Z-axis slice (nm)
ATP
ADP
0.0
0.5
1.0
A value
ADP
ATP
0.25
0.50
0.75
1.00
1.25
A value

Figure 4

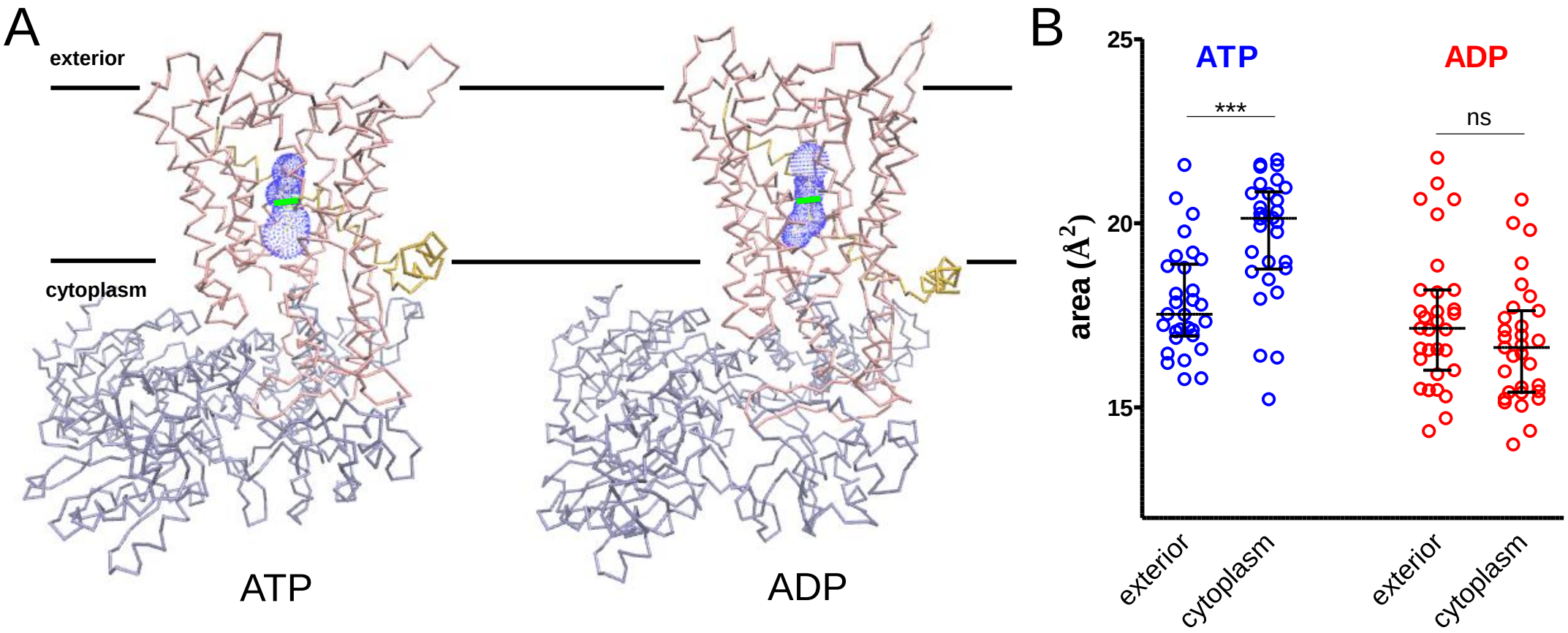
A
exterior
cytoplasm
ATP
ADP
B
ATP
ADP
***
ns
area (Å²)
25
20
15
exterior
cytoplasm
exterior
cytoplasm

Figure 5

A

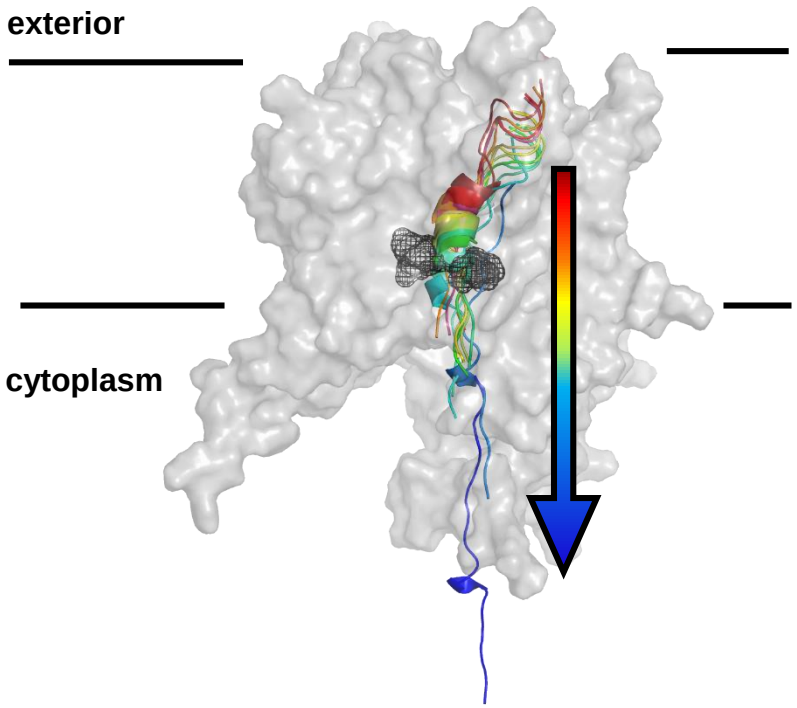
exterior
cytoplasm

B

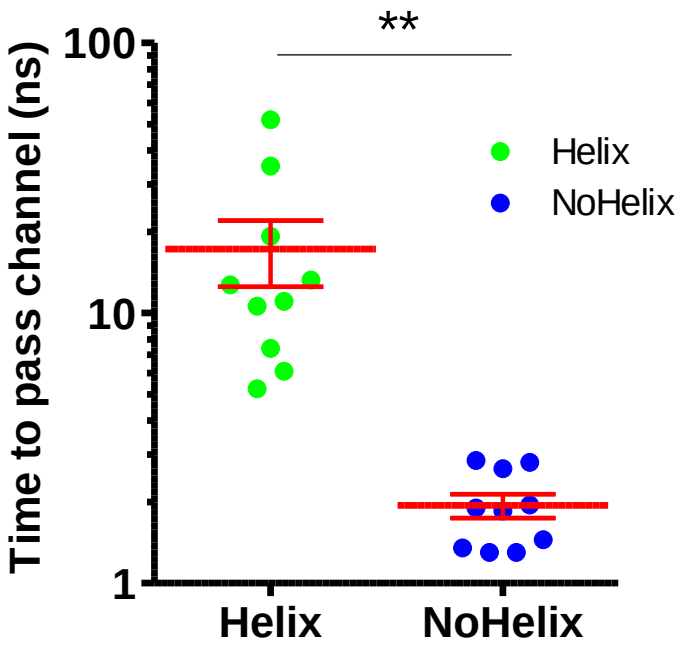
**
100
10
1
Time to pass channel (ns)
Helix
NoHelix
Helix
NoHelix

Figure 6

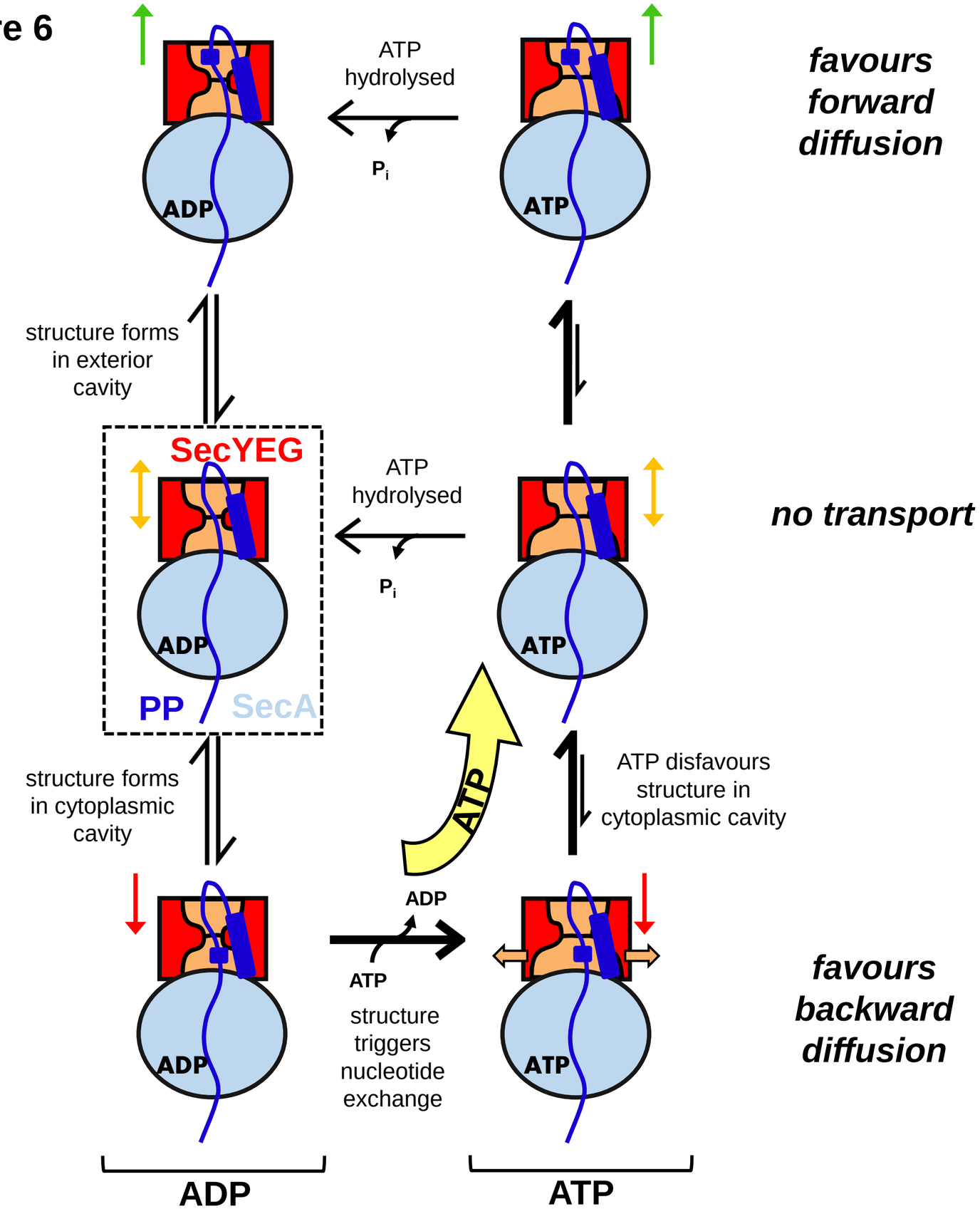
ATP
hydrolysed
P_i
ADP
ATP
favours
forward
diffusion
structure forms
in exterior
cavity
SecYEG
ATP
hydrolysed
P_i
ADP
ATP
no transport
PP
SecA
structure forms
in cytoplasmic
cavity
ATP
ATP disfavours
structure in
cytoplasmic cavity
ADP
ATP
structure
triggers
nucleotide
exchange
ADP
ATP
favours
backward
diffusion
ADP
ATP